

# Thermal and Damp Heat Stability of High-Mobility In<sub>2</sub>O<sub>3</sub>-Based Transparent Conducting Films Fabricated at Low Process Temperatures

Takashi Koida\* and Yuko Ueno

High electron mobility of transparent conductive oxide (TCO) facilitates high conductivity at a moderate carrier density, resulting in an extension of the degree of transparency from visible to near-infrared due to less free carrier absorption. These broadband TCO electrodes provide opportunities to improve the performance of optoelectronic devices. Herein, the thermal and damp heat stability characteristics of TCO films are described. It is found that the difference in the crystal growth method has a significant influence on the initial electrical properties and stability characteristics. Polycrystalline In<sub>2</sub>O<sub>3</sub>:Me (Me: W, Ce) films deposited at 200 °C exhibit a relatively high mobility of 70–80 cm<sup>2</sup> V<sup>−1</sup> s<sup>−1</sup>, are stable after a damp heat test, and improve the mobility of 110–140 cm<sup>2</sup> V<sup>−1</sup> s<sup>−1</sup> after postannealing at temperatures greater than the deposition temperature. Conversely, solid-phase crystallized In<sub>2</sub>O<sub>3</sub>:Me,H films prepared by postannealing amorphous films exhibit an extremely high mobility of 100–160 cm<sup>2</sup> V<sup>−1</sup> s<sup>−1</sup>; however, they exhibit reduced stability characteristics after the damp heat test and high-temperature annealing process compared to the polycrystalline films. The deterioration of the electrical properties increases as the hydrogen content in the films increases. The results suggest that polycrystalline and solid-phase crystallized films should be used properly, according to the device manufacturing processes.

## 1. Introduction


High-mobility transparent conductive oxides (TCOs) have attracted considerable attention as window electrodes of (opto) electronic devices, e.g., thin-film transistors, photosensors, light-emitting devices, and photovoltaics. The high electron mobility of TCO films facilitates high conductivity at a moderate carrier density, resulting in an extension of the degree of transparency from visible to near-infrared (NIR) due to less free carrier

absorption.<sup>[1–3]</sup> Therefore, these broadband TCO (BB-TCO) electrodes improve the performance of existing light-detection and emitting devices by the reduction of optical and electrical losses within the window electrodes,<sup>[2,3]</sup> and could create new functional devices such as NIR switching devices and image sensors with front irradiation.

For device integration, their realization in a conventional manufacturing process flow is crucial. The fabrication of TCO electrodes on heat-sensitive layers or substrates is typically constrained by the trade-off between fabrication temperatures and TCO properties. Historically, polycrystalline (*poly*-) Sn-doped indium oxide (ITO)<sup>[4–6]</sup> and amorphous (*a*-) In–Zn–O (IZO)<sup>[7,8]</sup> have been used as standard TCOs to exhibit moderate mobility ( $\approx 40$  cm<sup>2</sup> V<sup>−1</sup> s<sup>−1</sup>) at low fabrication temperatures ( $\approx 200$  °C). Recently, polycrystalline In<sub>2</sub>O<sub>3</sub> films with significantly greater mobilities have been reported: 1) *Poly*-In<sub>2</sub>O<sub>3</sub> films doped with metal (Me: Ti,<sup>[9,10]</sup> Zr,<sup>[9,11,12]</sup> Hf,<sup>[13]</sup> Mo,<sup>[9,14]</sup> W,<sup>[15,16]</sup> and Ce<sup>[16,17]</sup>) impurities instead of Sn

exhibit mobilities greater than  $\approx 80$  cm<sup>2</sup> V<sup>−1</sup> s<sup>−1</sup> and 2) solid-phase crystallized (*spc*-) H-doped In<sub>2</sub>O<sub>3</sub> (In<sub>2</sub>O<sub>3</sub>:H)<sup>[18]</sup> and In<sub>2</sub>O<sub>3</sub>:Me, H<sup>[16,17]</sup> films exhibit mobilities of  $\approx 160$  cm<sup>2</sup> V<sup>−1</sup> s<sup>−1</sup>. These high mobility values are found in *poly*- and *spc*-films with low Me contents. The mobilities of the *poly*-films doped with Mo,<sup>[19]</sup> W,<sup>[15]</sup> and Zr<sup>[12]</sup> on glass are comparable to those of the corresponding epitaxial films grown on yttria-stabilized zirconia substrates, while the *spc*-films exhibit higher mobility than the epitaxial In<sub>2</sub>O<sub>3</sub>:Me films.<sup>[20,21]</sup> Some mobility values exceed the calculated values based on a model for a single-crystalline In<sub>2</sub>O<sub>3</sub> semiconductor in which scattering from phonon and ionized impurities is taken into account.<sup>[21,22]</sup> We are aware of the issue but have made meticulous measurements and the outcomes are consistent.<sup>[12,20,23]</sup> The high mobility values of these films have been attributed to longer relaxation times due to the low scattering cross-section of the dopant impurities and reduced scattering from oxygen vacancies and/or interstitials.<sup>[12,17,18,24–26]</sup> Hybridization effects of the dopant atom with the In<sub>2</sub>O<sub>3</sub> conduction band states and the resulting low effective mass of free electrons even in the highly degenerated semiconductor have also been discussed as a possible origin of the high mobility.<sup>[24,27–30]</sup> Such high-mobility TCO films have been applied as the window electrodes of solar cells. The BB-TCO films

Dr. T. Koida,<sup>[†]</sup> Y. Ueno  
 Research Center for Photovoltaics  
 National Institute of Advanced Industrial Science and Technology  
 1-1-1, Umezono, Tsukuba 305-8568, Japan  
 E-mail: t-koida@aist.go.jp

 The ORCID identification number(s) for the author(s) of this article can be found under <https://doi.org/10.1002/pssa.202000487>.

<sup>[†]</sup>Present address: Research Institute for Energy Conservation, National Institute of Advanced Industrial Science and Technology, 1-1-1, Umezono, Tsukuba 305-8568, Japan

DOI: 10.1002/pssa.202000487

in the former group typically require a high growth temperature, greater than 300–400 °C,<sup>[26]</sup> to achieve such high mobility. They are applied in superstrate-type solar cells<sup>[31,32]</sup> with a configuration of glass/TCO/absorbing layers/metal, where the TCO layer is deposited on the glass substrate. Conversely, their application in substrate-type solar cells with a configuration of substrate/metal/absorbing layers/TCO, where the TCO layer is deposited on the absorbing layers, is limited<sup>[33]</sup> because the high growth temperature during TCO deposition typically degrades the underlying p–n junctions and/or passivation effects of the absorbing layers. However, careful control of the metal impurity concentration and oxygen stoichiometry within the TCO films enables the achievement of high mobility at low deposition temperatures of  $\approx 200$  °C.<sup>[9,13,16,17]</sup> Therefore, these BB-TCO films have the potential to be widely used in a variety of solar cells and other (opto)electronic devices. Conversely, successful applications in several types of solar cells have already been reported for BB-TCO films in the latter group. Such high mobility can be achieved at low process temperatures of 150–200 °C using two-step processes: deposition of amorphous or amorphous-rich films grown at low temperatures via magnetron sputtering,<sup>[18]</sup> reactive plasma deposition (RPD),<sup>[17]</sup> or atomic layer deposition<sup>[34]</sup> with a subsequent crystallization process by thermal annealing at greater than 150 °C. Their optical transmittance is considerably superior in both visible and NIR wavelengths when compared to widely used TCOs, including ITO, IZO, F-doped SnO<sub>2</sub>, and Al-doped ZnO,<sup>[35]</sup> and marginally superior when compared to the *poly*-In<sub>2</sub>O<sub>3</sub>:Me with high mobility.<sup>[16]</sup> This has resulted in a performance gain for Si heterojunction solar cells,<sup>[36–40]</sup> Cu(In, Ga)Se<sub>2</sub> solar cells and minimodules,<sup>[41,42]</sup> and tandem<sup>[43–45]</sup> solar cells. In these solar cells, low process temperatures are required in the TCO deposition as well as the subsequent metallization and encapsulation processes. In the production of silicon heterojunction solar cells, for example, the crystallization of the as-deposited TCO layers occurs during a cure process of Ag pastes at a temperature of  $\approx 200$  °C, which are screen-printed on the TCO layer. Consequently, the BB-TCO electrodes can be successfully integrated in a conventional manufacturing process flow. This has, however, required the investigation of several aspects in devices, including the influences of the roughness of the underlying layers,<sup>[41,46]</sup> postannealing conditions,<sup>[47]</sup> and contact resistances<sup>[37,48]</sup> on device performances.

Previously, we reported on high-mobility *poly*-In<sub>2</sub>O<sub>3</sub>:Me (Me: W, Ce), *spc*-In<sub>2</sub>O<sub>3</sub>:H, and *spc*-In<sub>2</sub>O<sub>3</sub>:Me,H films, focusing on the synthesis procedure at low temperatures and their optoelectrical properties in as-prepared states.<sup>[16]</sup> In this work, we investigate the thermal and damp heat (DH) stabilities of the BB-TCO films. The former information is crucial for integration of the BB-TCO electrodes to (opto)electronic devices that require metallization processes involving high temperatures. For example, devices including thin-film transistors, photosensors, light-emitting devices, and certain photovoltaics require a high-temperature process to reduce contact resistances and/or improve their device performance by the reduction of lattice and interface defects.<sup>[49–52]</sup> The latter information, the DH stability of the TCO films, is important for the design of device encapsulation. There have been reports on the stability of specific *spc*-TCO films without encapsulation under a hot and humid atmosphere,<sup>[53–56]</sup> however, the results reported by the different groups

vary. Herein, we investigate the DH stability characteristics for *poly*-films with extremely low H and *spc*-films with low and high H. The comparative studies reveal the origin of the variation and suggest an approach to achieve highly stable BB-TCO films.

## 2. Results and Discussion

### 2.1. Thermal Stability

**Figure 1** shows the resistivity ( $\rho$ ), carrier density ( $N$ ), and mobility ( $\mu$ ) values for a) *poly*- and b) *spc*-films with a thickness of  $\approx 220$  nm measured at room temperature after three Hall- $T$  measurements (50–300–50, 50–400–50, and 50–500–50 °C) in vacuum for the number of hours specified in the Experimental Section. In **Figure 1a**, the *poly*-In<sub>2</sub>O<sub>3</sub>:W and *poly*-In<sub>2</sub>O<sub>3</sub>:Ce films exhibit a decrease in  $\rho$  with a constant  $N$  and an increase in  $\mu$  when the films are postannealed at higher temperatures. The *poly*-In<sub>2</sub>O<sub>3</sub> film exhibits a different behavior;  $N$  monotonically decreases, whereas the  $\mu$  value increases first and then gradually decreases. Consequently,  $\rho$  increases after annealing at temperatures greater than 400 °C. A similar yet more striking trend is observed in the crystallized films. In **Figure 1b**, the *spc*-In<sub>2</sub>O<sub>3</sub>:H film exhibits a large decrease in  $N$ , whereas the  $\mu$  value marginally increases first and then rapidly decreases when the annealing temperature increases. A similar trend is observed in the *spc*-In<sub>2</sub>O<sub>3</sub>:W,H and *spc*-In<sub>2</sub>O<sub>3</sub>:Ce,H films; however, the increase in  $\rho$  is less than the *spc*-In<sub>2</sub>O<sub>3</sub>:H film due to the higher  $N$  and  $\mu$  values.

**Figure 2** shows the  $\rho$ ,  $N$ , and  $\mu$  values for a) *poly*- and b) *spc*-films with a thickness of  $\approx 60$  nm as a function of annealing temperature in N<sub>2</sub> for 30 min. Basically, both *poly*- and *spc*-films exhibit similar behavior to that observed in **Figure 1**; the *poly*-In<sub>2</sub>O<sub>3</sub>:Me films exhibit a decrease in  $\rho$  with an increase in  $\mu$ , whereas the *spc*-films exhibit an increase in  $\rho$  with decreases in  $N$  and  $\mu$ . Furthermore, the *poly*-In<sub>2</sub>O<sub>3</sub>:Me films exhibit similar  $\rho$ ,  $N$ , and  $\mu$  values in the as-deposited and postannealed states, regardless of the film thickness and annealing conditions. The *spc*-films also exhibit similar  $\rho$ ,  $N$ , and  $\mu$  values in the initial state regardless of the film thickness; however, the degradation in  $\rho$  in **Figure 2b** is considerably less than that in **Figure 1b**. The *spc*-films in **Figure 2b** exhibit a decrease in  $N$  with reduced slope compared to that in **Figure 1b**. Furthermore, the  $\mu$  value increases when the annealing temperature increases from 400 to 500 °C. This behavior is not observed in **Figure 1b**. In the *poly*-In<sub>2</sub>O<sub>3</sub> film, a degradation in  $\rho$  is observed by postannealing at 500 °C in a vacuum for the extended number of hours, whereas an improvement in  $\rho$  is observed by postannealing in N<sub>2</sub> for 30 min.

To summarize these results, the variation of the electrical properties by high-temperature annealing can be categorized into two groups. 1) The *poly*-In<sub>2</sub>O<sub>3</sub>:Me films exhibit improved electrical properties after postannealing. The properties are determined by the Me content and annealing temperature, rather than the film thickness and annealing time. 2) The *poly*-In<sub>2</sub>O<sub>3</sub> and all the *spc*-films exhibit a degradation of the electrical

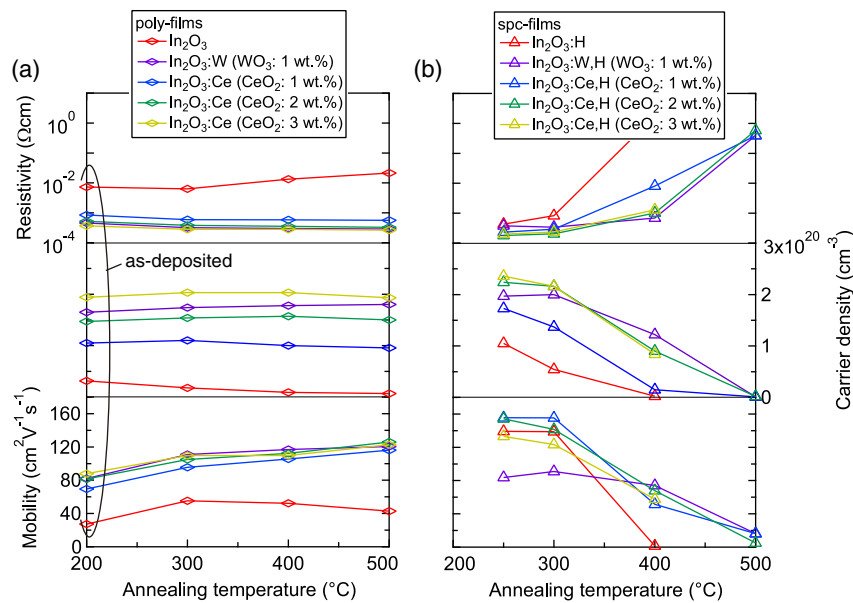


**Figure 1.** Resistivity, carrier density, and mobility values for a) *poly*- and b) *spc*-films with thickness of  $\approx 220$  nm as function of annealing temperature in vacuum for the extended number of hours.

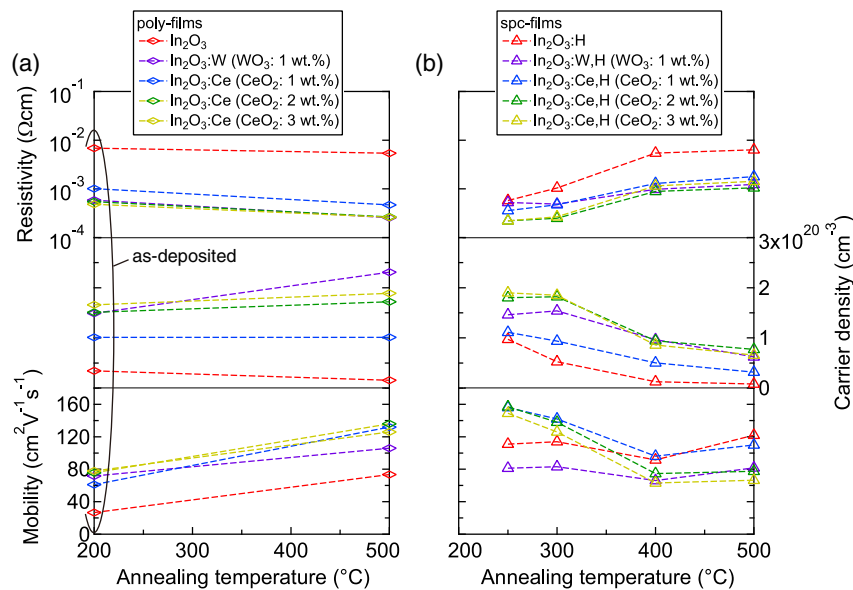


**Figure 2.** Resistivity, carrier density, and mobility values for a) *poly*- and b) *spc*-films with thickness of  $\approx 60$  nm as function of annealing temperature in  $\text{N}_2$  for 30 min.

properties. The degradation in  $N$  and  $\mu$  can be mitigated by metal doping and/or reducing the annealing time.

To investigate the origins of the variations in the electrical properties, we first characterized the structural properties of these films by X-ray diffraction (XRD), scanning electron microscopy (SEM), and thermal desorption spectroscopy (TDS). Then, we performed Hall and spectroscopic ellipsometry (SE) measurements for the films and compared their electrical and optical mobility to distinguish the influence of the postannealing on intra- and intergrain mobility.

Figure 3 shows the typical  $\theta$ - $2\theta$  XRD patterns of the a) *poly*- and b) *spc*-films in the initial and postannealed ( $T_a = 500$  °C) states as examples of *poly*- $\text{In}_2\text{O}_3$ , *poly*- $\text{In}_2\text{O}_3:\text{Ce}$  ( $\text{CeO}_2$ : 2 wt%), *spc*- $\text{In}_2\text{O}_3:\text{H}$ , and *spc*- $\text{In}_2\text{O}_3:\text{Ce,H}$  ( $\text{CeO}_2$ : 2 wt%) films with a thickness of  $\approx 220$  nm. Figure 3c plots the lattice spacings of the (222) plane ( $d_{222}$ ) and full-width at half-maximum ( $\text{FWHM}_{222}$ ) values of the 222 diffraction peaks for all the films. The XRD patterns do not indicate evidence of segregation of the tungsten and cerium oxides in the *poly*- $\text{In}_2\text{O}_3:\text{Me}$  and *spc*- $\text{In}_2\text{O}_3:\text{Me,H}$  films in either the initial or postannealed state. All of the *poly*-, *spc*- $\text{In}_2\text{O}_3:\text{H}$ , and

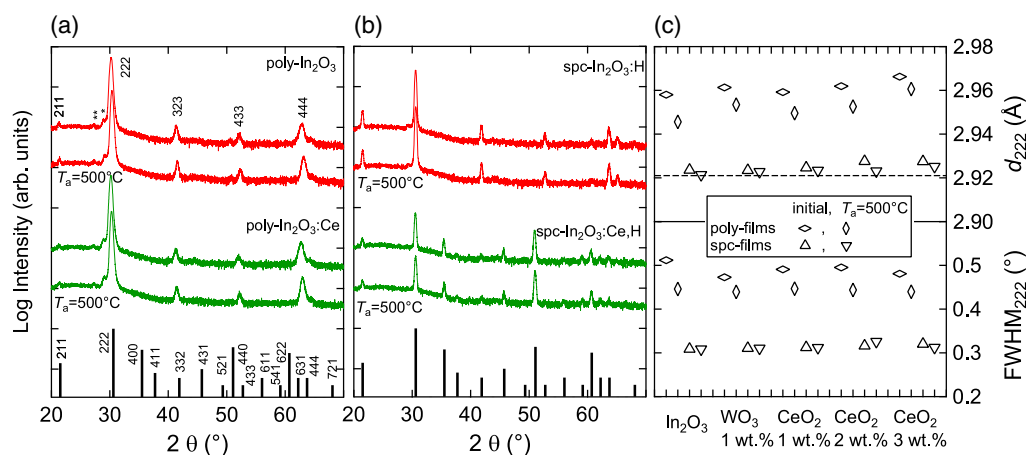


**Figure 3.**  $\theta$ - $2\theta$  XRD patterns of a) *poly*-In<sub>2</sub>O<sub>3</sub> and *poly*-In<sub>2</sub>O<sub>3</sub>:Ce (CeO<sub>2</sub>: 2 wt%), and b) *spc*-In<sub>2</sub>O<sub>3</sub>:H and *spc*-In<sub>2</sub>O<sub>3</sub>:Ce,H (CeO<sub>2</sub>: 2 wt%) films with thickness of  $\approx 220$  nm in initial and postannealed ( $T_a = 500^\circ\text{C}$ ) states. The two peaks denoted by “\*” and “\*\*” are 222 diffractions caused by Cu K $\beta$  and W-L lines caused by contamination of W from filaments, respectively. Stick patterns of In<sub>2</sub>O<sub>3</sub> (JCPDS-ICDD no. 6-416) are also shown for comparison. c) Lattice spacings of (222) plane ( $d_{222}$ ) and ( $\text{FWHM}_{222}$ ) values of (222) diffraction peaks for *poly*- and *spc*-films in initial and postannealed ( $T_a = 500^\circ\text{C}$ ) states.

*spc*-In<sub>2</sub>O<sub>3</sub>:Me,H films with low Me content exhibited 211, 222, 323, 433, and 444 reflections. The textures of the films were characterized on the basis of out-of-plane reciprocal space mapping and distribution of the poles for 222, 323, and 440 reflections<sup>[57]</sup> (refer to Figure S1, Supporting Information). The centers of gravity of the peaks for the 222 and 444 reflections were located on the coordinate of the reciprocal space in the direction perpendicular to the surface, whereas those of gravity of the peaks for 211, 323, and 433 were located in asymmetrical zones. These results prove that the films exhibited  $\langle 111 \rangle$  preferred orientation. The broadening of the 222 reflection along a circular path around the origin was  $\approx \pm 15^\circ$ . Due to the tilt and deviation of  $\langle 111 \rangle$  orientation from the surface normal direction, reflections of 211, 323, and 433 are observed in Figure 3. It should be noted that an in-line RPD system<sup>[58]</sup> was used to deposit the film on the substrate moving in a transport direction. The incidence angle of the deposition flux on the surface of the substrate gradually changed from  $\approx -14^\circ$  to  $14^\circ$  to the normal direction of the substrate, which could affect the tilt of  $\langle 111 \rangle$  orientation. By contrast, a randomly oriented structure was observed for the *spc*-In<sub>2</sub>O<sub>3</sub>:Ce,H films with high CeO<sub>2</sub> contents (2 and 3 wt%). The difference can be explained by the surface energies in In<sub>2</sub>O<sub>3</sub> and different nucleus formation in the *poly*- and *spc*-films.<sup>[16]</sup> More importantly, the  $d_{222}$  values of the *poly*-films are considerably greater than those of the In<sub>2</sub>O<sub>3</sub> powders ( $d_{222} = 0.2921$  nm), indicating the formation of in-plane compressive strains in the films. Postannealing decreases both the  $d_{222}$  and  $\text{FWHM}_{222}$  values, reflecting an increase in crystallite size and decrease in the strains inside the films. Conversely, the  $d_{222}$  and  $\text{FWHM}_{222}$  values of the *spc*-films are considerably less than those of the *poly*-films. The  $d_{222}$  values are marginally greater than those of the In<sub>2</sub>O<sub>3</sub> powders and become virtually identical after postannealing. These results indicate that the *spc*-films in the initial state possess extremely small in-plane compressive strains with large crystallite sizes and the postannealing relaxes the strains. Notably, the  $\text{FWHM}_{222}$  values for the *spc*-films are limited by the slit width used for the XRD measurements rather than the crystalline quality of the films.

Figure 4 shows the SEM images of the *poly*-In<sub>2</sub>O<sub>3</sub>, *poly*-In<sub>2</sub>O<sub>3</sub>:Ce (CeO<sub>2</sub>: 2 wt%), *spc*-In<sub>2</sub>O<sub>3</sub>:H, and *spc*-In<sub>2</sub>O<sub>3</sub>:Ce,H (CeO<sub>2</sub>: 2 wt%) films under different conditions: initial state, after three Hall-T measurements (50–300–50, 50–400–50, and 50–500–50 °C in a low vacuum for the extended number of hours), and after the TDS measurement (annealing up to  $\approx 700^\circ\text{C}$  in an ultrahigh vacuum with a ramping speed of  $\approx 16^\circ\text{C min}^{-1}$ ). In the initial state, the *poly*-films exhibit grain sizes of  $\approx 50$  nm, whereas the *spc*-films exhibit large grain sizes over 500 nm. This result is in acceptable agreement with the large difference in crystallite size between the *poly*- and *spc*-films revealed by the XRD measurements. Each grain exhibited single orientation, as revealed by the electron backscatter diffraction (EBSD) and transmission electron microscope (TEM) analyses (refer to Figure S2 and S3, Supporting Information, and Koida et al.<sup>[16]</sup>). The *poly*-films exhibit no large change in grain size after postannealing at 500 and  $\approx 700^\circ\text{C}$ . Conversely, the *spc*-films exhibit the formation of small precipitates with a high density on the grain surfaces and large precipitates with a low density at the grain boundaries (GBs) after the Hall-T measurements, whereas the films exhibit void spaces on the surfaces and large void spaces at the GBs without the formation of precipitates after the TDS measurement. We performed composition analysis using an electron probe microanalyzer (EPMA) for the *spc*-films and found that no condensation of Ce, W, or In metal occurs at the precipitates. These results suggest that the formation of precipitates is induced by the diffusion of excess In to the grain surfaces that are not soluble within a crystal grain at an annealing temperature.<sup>[59]</sup> We assume that extended-time low-vacuum annealing promotes oxidation of the excess In at the surfaces by water and/or residual O<sub>2</sub> gas in the low vacuum to form indium oxide, whereas rapid thermal annealing at high temperatures under an ultrahigh vacuum promotes effusion of the volatile species, including the excess In and H<sub>2</sub>O from the surface without the formation of the precipitates. The latter phenomenon was detected by TDS spectra.

TDS analysis reveals large difference in the effusion behavior between the *poly*- and *spc*-films. Figure 5 displays the TDS spectra



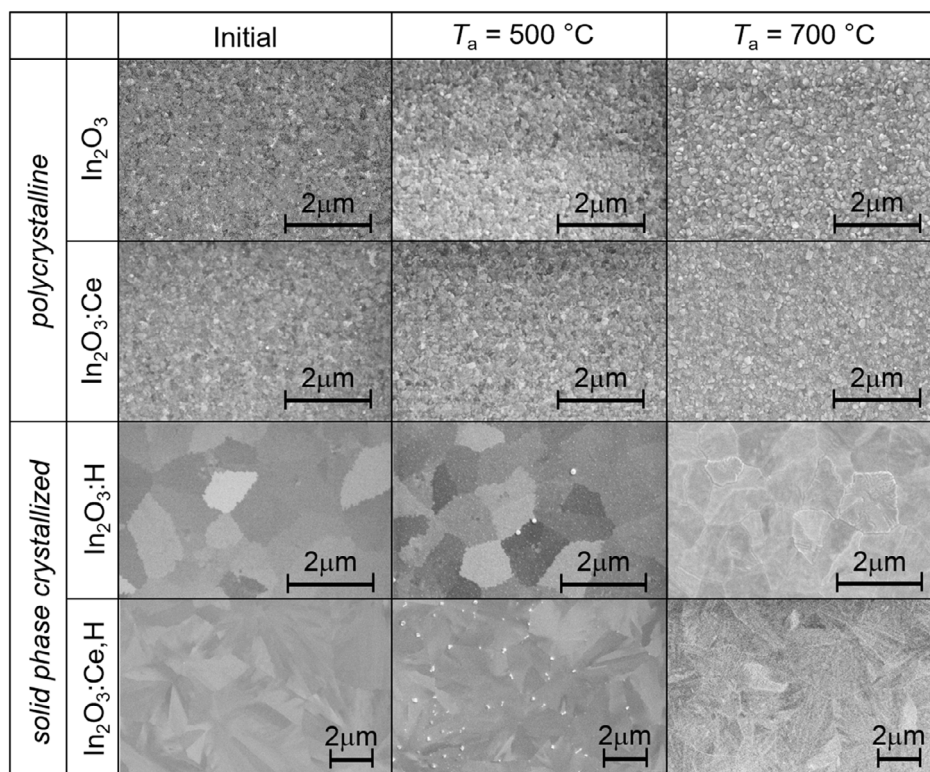


**Figure 4.** SEM images of *poly*- $\text{In}_2\text{O}_3$ , *poly*- $\text{In}_2\text{O}_3:\text{Ce}$  ( $\text{CeO}_2$ : 2 wt%), *spc*- $\text{In}_2\text{O}_3:\text{H}$ , and *spc*- $\text{In}_2\text{O}_3:\text{Ce,H}$  ( $\text{CeO}_2$ : 2 wt%) films in initial state, after three Hall-T measurements (50–300–50, 50–400–50, and 50–500–50 °C in low vacuum for the extended number of hours), and after TDS measurement (annealing up to  $\approx 700\text{ }^\circ\text{C}$  in ultra-high vacuum with ramping speed of  $\approx 16\text{ }^\circ\text{C min}^{-1}$ ).

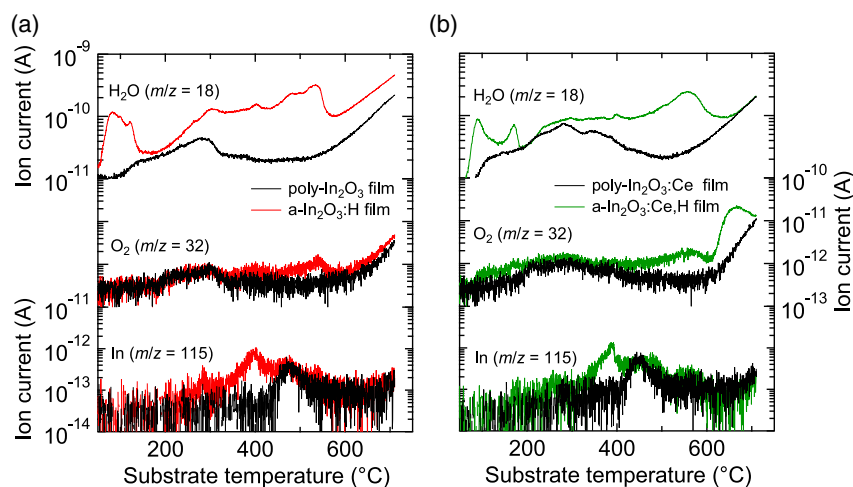


**Figure 5.** TDS spectra of desorbed species from a) *poly*- $\text{In}_2\text{O}_3$  and *a*- $\text{In}_2\text{O}_3:\text{H}$  films, and b) *poly*- $\text{In}_2\text{O}_3:\text{Ce}$  ( $\text{CeO}_2$ : 2 wt%) and *a*- $\text{In}_2\text{O}_3:\text{Ce,H}$  ( $\text{CeO}_2$ : 2 wt%) films.

of the desorbed species from the a) *poly*- $\text{In}_2\text{O}_3$  and *a*- $\text{In}_2\text{O}_3:\text{H}$  films and b) *poly*- $\text{In}_2\text{O}_3:\text{Ce}$  ( $\text{CeO}_2$ : 2 wt%) and *a*- $\text{In}_2\text{O}_3:\text{Ce,H}$  ( $\text{CeO}_2$ : 2 wt%) films. Water molecules desorb from the *poly*-films and the effusion terminates at a temperature of  $\approx 500\text{ }^\circ\text{C}$ . Here, the increase in the signal above 500–600 °C is considered to be outgassing from the sample stage by the readsorption of previously desorbed gasses. The H content in the initial *poly*-films was

0.2–0.5 at%, as estimated by the TDS and hydrogen forward scattering spectroscopy measurements.<sup>[16]</sup> Conversely, a considerably greater number of water molecules effuse from the *a*-films. The H contents were 1.7 and 2.0 at% in the initial *a*- $\text{In}_2\text{O}_3:\text{H}$  and *a*- $\text{In}_2\text{O}_3:\text{Ce,H}$  films, respectively.<sup>[16]</sup> The details of the effusion behavior are explained elsewhere.<sup>[25]</sup> Specifically, there are two large  $\text{H}_2\text{O}$  desorption peaks at temperatures less than 200 °C;

the second  $\text{H}_2\text{O}$  peak occurs with crystallization of the films. Even after the crystallization, the desorption of a large amount of  $\text{H}_2\text{O}$  is detected from the *spc*-films at temperatures up to  $\approx 600^\circ\text{C}$ . These results demonstrate that 1) H is present inside the crystal grains and 2) excess H that is not soluble inside the crystal grains at an annealing temperature diffuses out to the grain surfaces and GBs to form the  $\text{H}_2\text{O}$  gasses. These are consistent with the analysis from atom probe tomography for  $\text{In}_2\text{O}_3$ :H films in the initial and postannealed states.<sup>[60]</sup> Here, we assume that the configurations of the H in the *spc*- $\text{In}_2\text{O}_3$  films are  $\text{H}_\text{O}$ ,  $\text{H}_\text{i}$ , and  $\text{OH}_\text{O}$  within the crystalline grains<sup>[61,62]</sup> and OH groups at dislocations and the GBs.<sup>[62–64]</sup> In Figure 5, small In desorption peaks at  $\approx 400$ , 480, and  $530^\circ\text{C}$  are detected without remarkable  $\text{O}_2$  desorption peaks, indicating the existence of excess In within the films that were deposited under a slightly oxygen-poor condition.<sup>[65]</sup>

In the following segment, we discuss the variation of the electrical properties in Figure 1, based on the results of the structural properties. 1) *Poly*-films: The initial films exhibit a granular structure with a size of  $\approx 50$  nm and in-plane compressive strains. The films have a H content of 0.2–0.5 at%. The films postannealed at  $500^\circ\text{C}$  exhibit a similar structure with no large change in the grain size. However, a marginal increase in crystallite size and similar decrease in in-plane compressive strains can be observed by XRD measurement. The  $\mu$  values gradually increase with constant  $N$  values for the *poly*- $\text{In}_2\text{O}_3$ :Me films. These results clearly demonstrate that the improvement in  $\mu$  is a consequence of the improved crystallinity by postannealing, and metal impurities that generate free carriers in these films are solid-soluble in both the initial and postannealed states at  $500^\circ\text{C}$ . Conversely, the *poly*- $\text{In}_2\text{O}_3$  film exhibits a monotonical decrease in  $N$  with a first increase and subsequent decrease in  $\mu$ . The decrease in  $N$  can be explained by the effusion of the H and OH that work as electron donors<sup>[61,62]</sup> and passivate acceptor defects.<sup>[66]</sup> The reduction of the donors should increase the  $\mu$  values due to less ionized impurity scattering. Indeed, the  $\mu$  value marginally increases after annealing at  $300^\circ\text{C}$ . However, the  $\mu$  value decreases with  $N$  after higher temperature annealing. The result clearly indicates that additional defects including the acceptor defects are also formed at temperatures greater than  $400^\circ\text{C}$ . This phenomenon is more striking for the *spc*-films, as described later. Notably, the *poly*- $\text{In}_2\text{O}_3$  film postannealed in  $\text{N}_2$  for 30 min (Figure 2a) exhibits less decrease in  $N$  with an increase in  $\mu$  when compared to the thicker film postannealed in a vacuum for the extended number of hours. The improved electrical properties can be explained by reduced effusion of  $\text{H}_2\text{O}$  from the films due to the milder postannealing condition. This effusion also occurs in the *poly*- $\text{In}_2\text{O}_3$ :Me films. However, the decrease in  $N$  and  $\mu$  for the films is largely masked by the large number of metal donors with the improvement of crystallinity by postannealing. 2) *Spc*-films: The initial films exhibit large grain structure over 500 nm with high crystallinity and less in-plane compressive strains. The films have H contents of 1.4–2.0 at%. During postannealing at  $500^\circ\text{C}$ , large amounts of H, OH, and In-related species diffuse to the grain surfaces and the corresponding gasses are effused from the films through the GBs and grain surfaces. The films exhibit negligible in-plane compressive strains, likely due to the formation of nanospaces at the GBs where the gases effused during postannealing. The initial *spc*-films exhibit extremely high  $\mu$  values, reflecting

low impurity scattering within the grains and low GB scattering.<sup>[18,22,25,67,68]</sup> However, postannealing at temperatures greater than  $400^\circ\text{C}$  reduces both the  $N$  and  $\mu$  values. The free carriers generated by the H, OH, and Me impurities in the initial *spc*-films significantly decrease with the effusion of  $\text{H}_2\text{O}$ . The resulting  $N$  values are considerably less than those of the corresponding *poly*-films where Me impurities are considered to generate free carriers. These results clearly demonstrate that 1) low impurity and GB scattering in the initial *spc*-films are achieved by passivation of the lattice defects by large amounts of H while maintaining high crystallinity and 2) diffusion of the H and OH by high-temperature annealing produces lattice defects inside the grains, leading to strong carrier compensation. The degradation of the electrical properties at high temperatures can be mitigated by shorter time annealing in  $\text{N}_2$  due to less  $\text{H}_2\text{O}$  effusion from the films, as observed in the *poly*-films.

To distinguish the effects of inter- and intragrain properties on the mobility, we compared the Hall mobility with the optical mobility ( $\mu_\text{opt}$ ) determined by SE measurements. In the *poly*- and *spc*-films, the grain sizes are far larger than the mean free path of free electrons<sup>[25,69]</sup> and the electrons need to cross GBs. This is in most cases a thermally activated process as potential barriers form due to charged defects at GBs. In this work, we used the approach adapted by Frischbier for characterizing GB potential barriers in TCO films,<sup>[70]</sup> wherein the mobility in the films is expressed by  $\mu = \mu_\text{IG} \times \exp(E_\text{B}/k_\text{B}T)$ .<sup>[71,72]</sup> Here,  $\mu_\text{IG}$ ,  $E_\text{B}$ ,  $k_\text{B}$ , and  $T$  are the intragrain mobility, GB potential barrier height, Boltzmann constant, and temperature, respectively. The intragrain mobility is generally determined by scattering processes produced by impurities and phonons. We use  $\mu_\text{opt}$  as  $\mu_\text{IG}$  in this study because, in optical characterization, the charge carriers are accelerated by an AC electric (and magnetic) field and the resulting range of motion from the classical point of view for the applied frequency region is considerably smaller than the typical grain size of the films. Thus, the GBs influence the electronic motion significantly less and  $\mu_\text{opt}$  can be considered as the intragrain mobility without the contribution of the GBs. **Figure 6** plots the optical carrier density ( $N_\text{opt}$ ) and  $\mu_\text{opt}$  values obtained by SE measurements for the  $\approx 60$  nm thick a) *poly*- and b) *spc*-films before and after postannealing at  $500^\circ\text{C}$  in  $\text{N}_2$ . At a glance, the variations in the  $N_\text{opt}$  and  $\mu_\text{opt}$  as a function of the annealing temperature are similar to those in electrical carrier density and mobility in both the *poly*- and *spc*-films (Figure 2). To carefully investigate the effect of postannealing on intergrain properties, we plot  $\mu/\mu_\text{opt}$  and  $E_\text{B}$  values for the *poly*- and *spc*-films as a function of annealing temperature in **Figure 7a,b**, respectively.

In Figure 6a, the  $\mu_\text{opt}$  values for all the *poly*-films increase by postannealing, proving that postannealing improves intragrain properties. This improvement is attributed to the structural improvement discussed previously. However, the  $\mu_\text{opt}$  values for the *poly*- $\text{In}_2\text{O}_3$ :Ce ( $\text{CeO}_2$ : 2, 3 wt%) films postannealed at  $500^\circ\text{C}$  remain less than those of the *spc*-films in the initial state, indicated in Figure 6b. This result suggests that there is the possibility to further improve the intragrain properties by postannealing at higher temperatures. Conversely, the  $\mu/\mu_\text{opt}$  values in Figure 7a increase by postannealing and approach 1 for the *poly*-films. As a result, the  $E_\text{B}$  values decrease from a few millielectronvolts to 0. This result clearly demonstrates that postannealing also reduces the defect density at the GBs and regions

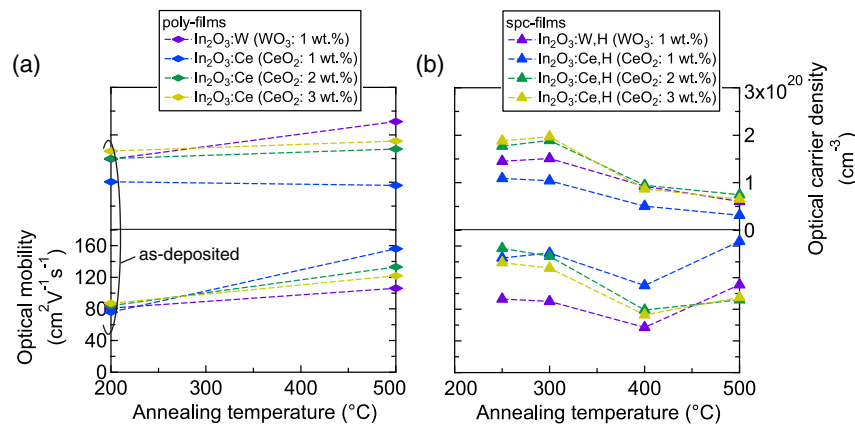


**Figure 6.** Optical carrier density and optical mobility of  $\approx 60$  nm thick a) *poly*- and b) *spc*-films before and after postannealing at 500 °C in  $N_2$ .

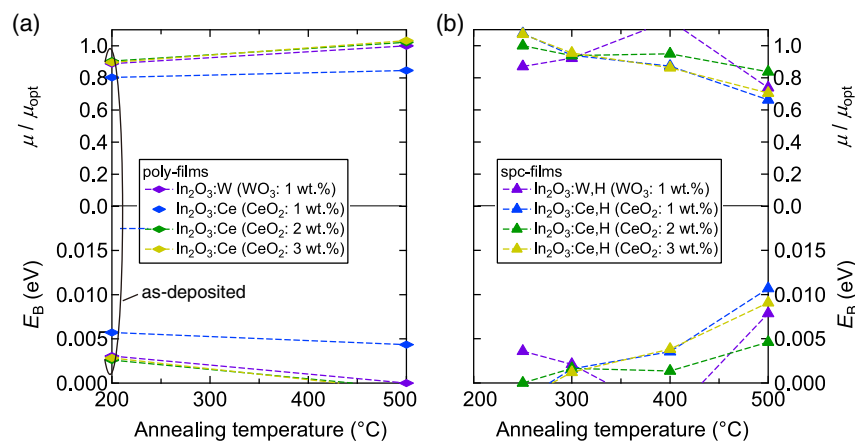


**Figure 7.**  $\mu/\mu_{\text{opt}}$  values and grain boundary barrier heights ( $E_B$ ) for  $\approx 60$  nm thick: a) *poly*- and b) *spc*-films as function of annealing temperature.

close to the GBs, leading to the negligible influence of GB scattering on their transport. We assume that there is a reconstruction around the GBs by postannealing causing this improvement, although we could not observe a clear change in structure by the high-resolution TEM analysis. (refer to Figure S3, Supporting Information) Similar phenomena have also been reported in ZnO:Al films postannealed at temperatures greater than growth temperatures.<sup>[73,74]</sup> It should be noted that the marginally higher  $E_B$  value in the *poly*- $\text{In}_2\text{O}_3$ :Ce ( $\text{CeO}_2$ : 1 wt.%) film can be explained by the fact that the GB defects continue to exist even after the postannealing and form a potential barrier due to reduced carrier density in the film. Conversely, *spc*-films exhibit different  $\mu/\mu_{\text{opt}}$  and  $E_B$  behaviors in Figure 7b; the  $\mu/\mu_{\text{opt}}$  values are approximately 1 in the initial state and gradually decrease with an increase in annealing temperature. The  $E_B$  values increase from 0 to  $\approx 10$  meV at 500 °C. This result demonstrates that effusion of  $\text{H}_2\text{O}$  from the films by postannealing activates passivated defects and/or produces additional defects at the GBs, producing a potential barrier for the free electrons.

In general, when the films are postannealed at high temperatures, the effect of segregation of metal dopants to GBs on their transport properties should be considered. The segregation energies also depend on crystal orientations.<sup>[63]</sup> Frischbier et al. have

reported that polycrystalline ITO films with a Sn dopant concentration over 2 wt% exhibit enhanced barrier heights ( $\approx 27$  meV) compared to nominally undoped and 0.5 wt% Sn-doped and 1 and 2 wt% Zr-doped  $\text{In}_2\text{O}_3$  films ( $\approx 20$  meV) with similar carrier densities of  $\approx 10^{20} \text{ cm}^{-3}$ .<sup>[70]</sup> In this study, the W-to-In atomic ratio was as low as 0.39 at% in the  $\text{In}_2\text{O}_3$ :W,H ( $\text{WO}_3$ : 1 wt.%) films, and the Ce-to-In ratios were as low as 0.28, 0.96, and 1.3 at% in the  $\text{In}_2\text{O}_3$ :Ce,H ( $\text{CeO}_2$ : 1, 2, and 3 wt.%) films, respectively.<sup>[16]</sup> Analysis of EPMA revealed that no condensation of Ce and W was observed at GBs for the *spc*-films postannealed at 500 °C regardless of the preferred orientations in the films. Furthermore, *spc*- $\text{In}_2\text{O}_3$ :H films without the metal dopants also exhibit similar decrease in  $\mu$  (Figure 1b and 2b). Therefore, neither the metal segregation nor orientation effects can explain the increase in the GB potential barrier height in this study.

Based on these results, the *poly*- and *spc*-films should be used properly according to the manufacturing process of the (opto)electric devices, including thin-film transistors, photosensors, light-emitting devices, and photovoltaics. Certain devices must withstand metallization processes involving high temperatures up to 400–500 °C. In these devices, it is critical to use a TCO layer that can endure high-temperature heat treatment while maintaining high electron mobility. The *poly*- $\text{In}_2\text{O}_3$ :Me layers

could be applied to such devices. After the heat treatment, their optoelectrical properties further improve. Conversely, other devices, including Si heterojunction solar cells and substrate-type thin-film solar cells, require a low-temperature (less than 200 °C) process during and after TCO formation to prevent degradation of the p–n junction and/or passivation effects of the absorbing layers. The *spc*-In<sub>2</sub>O<sub>3</sub>:Me,H layers could be applied to such devices. It should be noted that the *poly*-In<sub>2</sub>O<sub>3</sub>:Me and *spc*-In<sub>2</sub>O<sub>3</sub>:Me,H films were fabricated separately by changing the deposition temperatures and postdeposition process. In this study, we investigate completely polycrystalline films in as-deposited states or completely crystallized films from amorphous structures to investigate the characteristics of the thin films at both extremes. However, we could fabricate films with mixed phases composed of a crystalline phase in an as-deposited state and crystallized phase after postannealing by depositing at a marginally higher growth temperature and subsequent postannealing.<sup>[5,48]</sup> Such films would exhibit properties between the *poly*- and *spc*-films discussed herein. Therefore, films with mixed phases can also be used depending on the manufacturing process conditions of the applied devices.

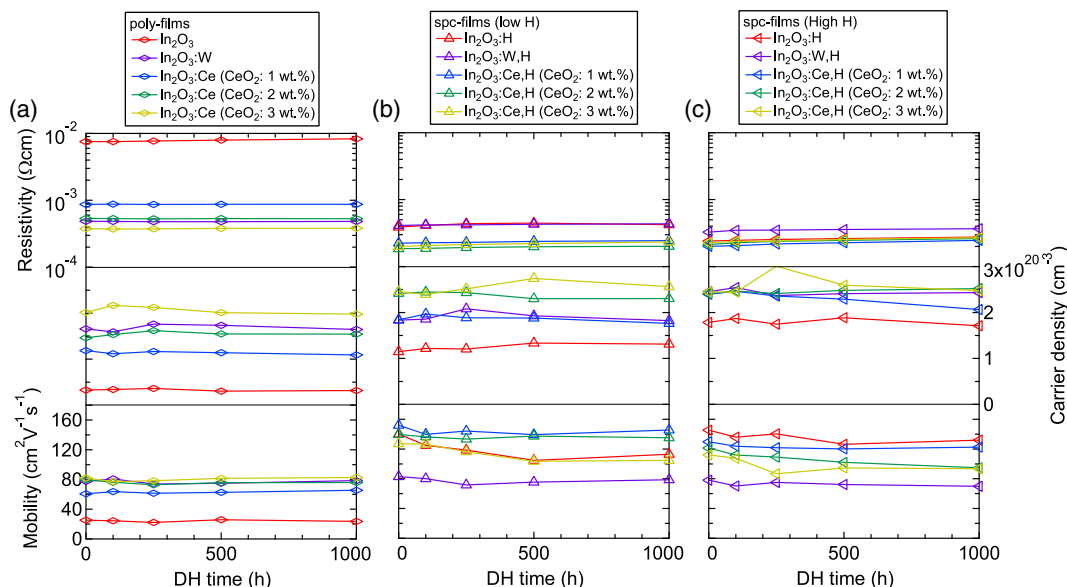
## 2.2. Damp Heat Stability

Figure 8 shows the variation of  $\rho$ ,  $N$ , and  $\mu$  values for the  $\approx 220$  nm thick a) *poly*-films with extremely low H (0.2–0.5 at%), b) *spc*-films with low H (1.4–2.0 at%), and c) *spc*-films with high H (2.4–3.7 at%) as a function of DH time. To clearly indicate the variation from the initial values, Figure 9 displays the  $\Delta\rho/\rho$ ,  $\Delta N/N$ , and  $\Delta\mu/\mu$  values with DH time. As shown in Figure 8a and 9a, *poly*-In<sub>2</sub>O<sub>3</sub>:W and *poly*-In<sub>2</sub>O<sub>3</sub>:Ce films exhibit stability under the DH test. No increase in  $\Delta\rho/\rho$  is observed for the films, whereas an  $\approx 10\%$  increase in  $\Delta\rho/\rho$  is observed for the *poly*-In<sub>2</sub>O<sub>3</sub> after 1000 h, primarily because of the decrease in  $\mu$ . Conversely, all the *spc*-films exhibit an increase in  $\Delta\rho/\rho$  with DH time, due to a decrease in  $\mu$ . The  $\Delta\rho/\rho$  values increase with the H content; the

*spc*-films with low H exhibit an  $\approx 10\%$  increase in  $\Delta\rho/\rho$  after 1000 h, whereas the *spc*-films with high H exhibit an  $\approx 20\%$  increase in  $\Delta\rho/\rho$  (Figure 9b,c).

Figure 10 shows the variation of the  $\rho$ ,  $N$ , and  $\mu$  values for the  $\approx 60$  nm thick a) *poly*-films with extremely low H, b) *spc*-films with low H, and c) *spc*-films with high H as a function of DH time. The trend of the variations in electrical properties is similar to that displayed in Figure 8, although the thinner *spc*-films exhibit a greater decrease in  $\mu$ , and a resulting greater increase in  $\rho$  after the DH test when compared to the thicker *spc*-films. Now, we focus on the inter- and intragrain mobility on the variation in  $\mu$  values. Figure 11 plots the  $N_{\text{opt}}$  and  $\mu_{\text{opt}}$  values for a) *poly*-films with extremely low H, b) *spc*-films with low H, and c) *spc*-films with high H as a function of DH time. Figure 12 shows the  $\mu/\mu_{\text{opt}}$  and  $E_{\text{B}}$  values calculated from the  $\mu$  and  $\mu_{\text{opt}}$  values. In the initial state, the  $\mu$  values for the majority of the films are equal to the  $\mu_{\text{opt}}$  values. The  $E_{\text{B}}$  values are less for the *poly*-films and close to zero for the *spc*-films, demonstrating the negligible influence of GB scattering on the  $\mu$  values. After the DH test, no large change in the  $\mu$ ,  $\mu_{\text{opt}}$ , and  $E_{\text{B}}$  values is observed for the *poly*-In<sub>2</sub>O<sub>3</sub>:Me films (Figure 10a, 11a, and 12a). These results demonstrate that the DH test induced negligible change in the inter- and intragrain properties. Conversely, the *spc*-films exhibit different behavior in Figure 10b,c, 11b,c, and 12b,c. After the DH test, only  $\mu$  decreases with no change in  $\mu_{\text{opt}}$ , suggesting that the DH test induces degradation of the intergrain properties with negligible change in the intragrain properties. The  $\mu$  values decrease significantly for the *spc*-films with high H. Moreover, the  $\mu$  values decrease and the  $E_{\text{B}}$  values increase systematically with the decreasing  $N$  values for the *spc*-films with high H. This behavior can be explained by a decreasing  $N$ , which reduces the transport by creating a higher and wider potential barrier at the GBs.

The relatively large difference in DH stability characteristics among the *poly*-films, *spc*-films with low H, and *spc*-films with high H is attributed to the different degree of water-molecule



**Figure 8.** Resistivity, carrier density, and mobility values for  $\approx 220$  nm thick a) *poly*-films with extremely low H (0.2–0.5 at%), b) *spc*-films with low H (1.4–2.0 at%), and c) *spc*-films with high H (2.4–3.7 at%) as function of DH time.



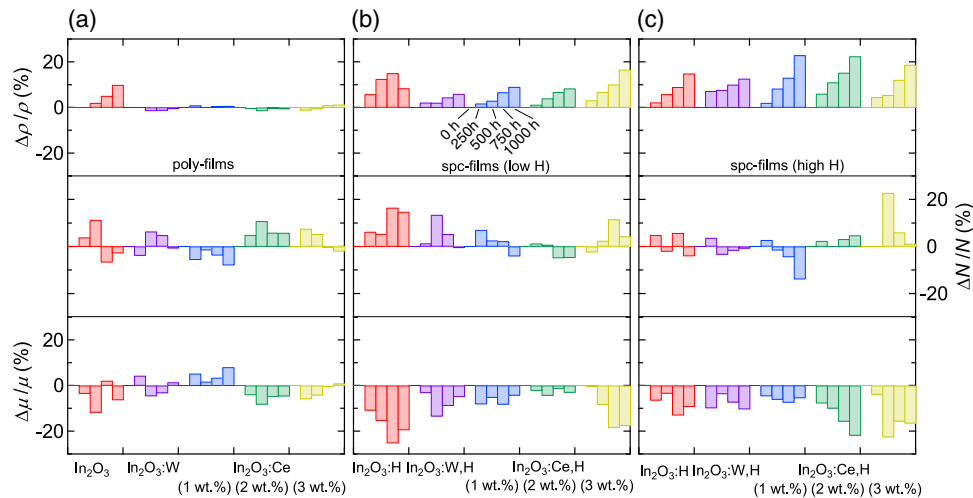


**Figure 9.** Variation of resistivity, carrier density, and mobility from initial values for  $\approx 220$  nm thick a) *poly*-films with extremely low H (0.2–0.5 at%), b) *spc*-films with low H (1.4–2.0 at%), and c) *spc*-films with high H (2.4–3.7 at%) as function of DH time.

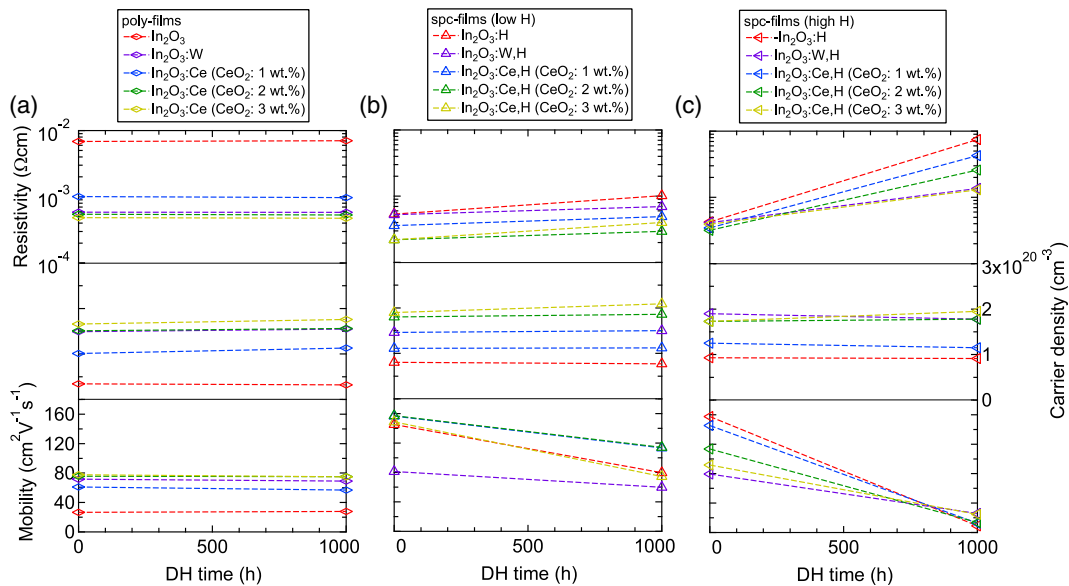


**Figure 10.** Resistivity, carrier density, and mobility values for  $\approx 60$  nm thick a) *poly*-films with extremely low H, b) *spc*-films with low H, and c) *spc*-films with high H before and after DH test.

ingress into the GBs caused by spaces at the GBs. The *poly*-films possess in-plane compressive strains and the crystalline grains are densely packed. Therefore, there are no spaces for water molecules to ingress through the GBs. Conversely, *spc*-films possess small in-plane compressive strains with reducing strains as the H content increases. Moreover, the effusion of  $\text{H}_2\text{O}$  through the GBs from the films increases with the H at temperatures up to  $250^\circ\text{C}$ . Therefore, we can assume that the *spc*-films possess void spaces at the GBs that are comparable to the molecular size of water. The size of the void spaces would increase with the H content in the as-deposited films because the crystallized grains cannot accommodate the large amount of vacancies originating from the diffusion of the H- and OH-related species within the

lattices while maintaining a constant GB space. Due to the spaces at the GBs,  $\text{H}_2\text{O}$ ,  $\text{CO}_2$ , and other atmospheric constituents could penetrate through the GBs in the *spc*-films during the DH test. A DFT calculation of the configurations of adsorbed water molecules on the  $\text{In}_2\text{O}_3(111)$  surface at 300 K suggests that absorbed water molecules on the  $\text{In}_2\text{O}_3$  surface under low water partial pressure ( $<10^{-4}$  mbar) readily split into  $\text{H}^+$  and  $\text{OH}^-$ , which bond with the oxygen and indium ions in the  $\text{In}_2\text{O}_3$ , respectively. Higher water coverages, which include three dissociated water molecules and six molecules, absorb in the  $(1 \times 1)$  unit cell of the  $\text{In}_2\text{O}_3(111)$  under high water partial pressure ( $>10^{-2}$  mbar).<sup>[64]</sup> Therefore, a high coverage of water molecules would appear at the GBs in the DH test. We can assume that the

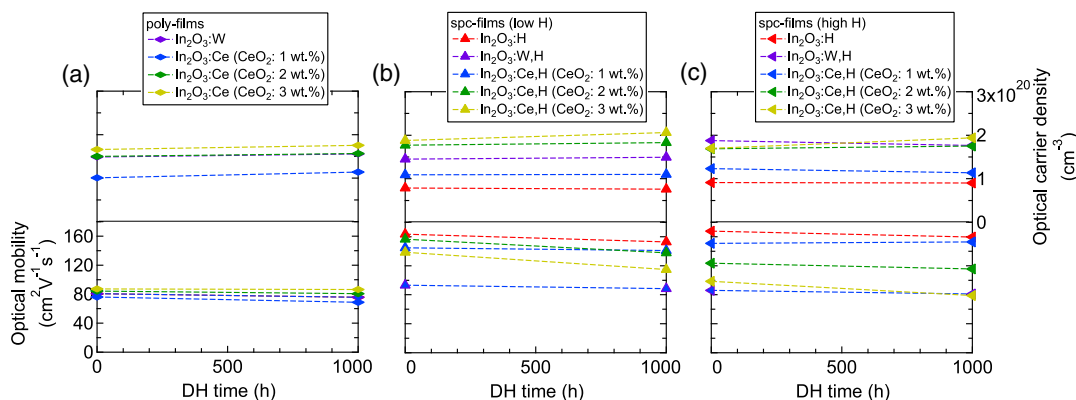


**Figure 11.** Optical carrier density and optical mobility of  $\approx 60$  nm thick a) *poly*-films with extremely low H, b) *spc*-films with low H, and c) *spc*-films with high H before and after DH test.

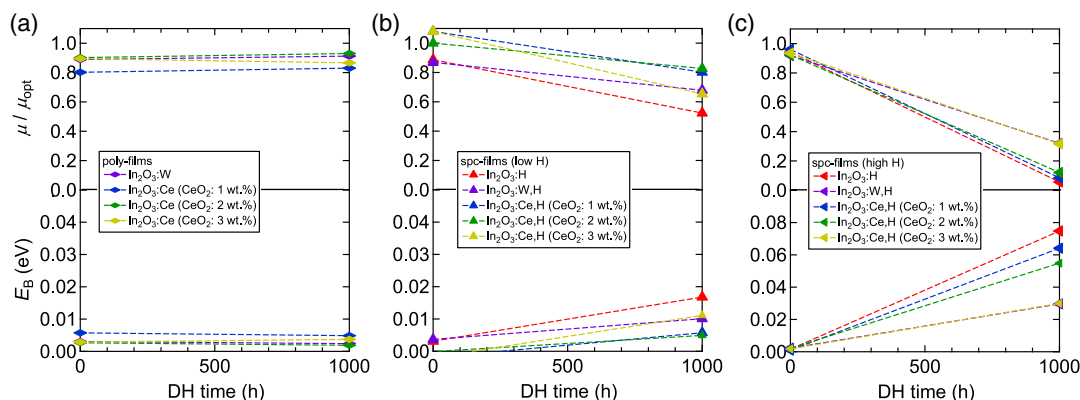


**Figure 12.**  $\mu/\mu_{opt}$  values and grain boundary barrier heights ( $E_B$ ) for  $\approx 60$  nm thick a) *poly*-films with extremely low H, b) *spc*-films with low H, and c) *spc*-films with high H before and after DH test.

initial grain surfaces and GBs prepared by postannealing are terminated by the dissociated water molecules,<sup>[62–64]</sup> which passivate surface defects, whereas the additional absorbed water molecule layers formed during the DH test create a potential barrier for electrons at the GBs. This idea is consistent with the fact that the degradation is virtually completely reversible by a repetition of the vacuum annealing step at 200 °C.<sup>[55]</sup> Chemical bonds such as hydroxides or carbonates that form at the GBs are also thought to impair the passivated GBs by the H.<sup>[55]</sup> The absorption of OH radicals during the DH test is thought to disrupt the H at the GBs from forming H<sub>2</sub>O molecules.<sup>[54]</sup>

Based on these results, dense GB structures are crucial to achieving stable films under a hot and humid atmosphere. Notably, the  $\approx 220$  nm thick *spc*-films with smaller lateral grain sizes exhibit less degradation than the  $\approx 60$  nm thick *spc*-films. Moreover, the  $\approx 220$  nm thick *spc*-films prepared by magnetron sputtering possessing smaller lateral grain sizes exhibit more stability than those prepared by RPD.<sup>[56]</sup> Therefore, the density of the GBs and position of the GBs against current flow direction influence the DH degradation. As described previously, we can fabricate films with mixed phases composed of a crystalline phase in an as-deposited state and crystallized phase after post-annealing, by changing the growth temperature. Such films with denser GB structures would exhibit

superior properties when compared to the *spc*-films. In this study, we focused on the stability issues of the TCO layer itself; however, there are several additional approaches to prevent degradation, for example, by a lamination technique or the overcoating of a barrier layer such as SiN<sub>x</sub> in device integration.

### 3. Conclusion

We investigated the thermal and DH stability characteristics of high-mobility *poly*-In<sub>2</sub>O<sub>3</sub>:Me (Me: W, Ce), *spc*-In<sub>2</sub>O<sub>3</sub>:H, and *spc*-In<sub>2</sub>O<sub>3</sub>:Me,H films fabricated at low process temperatures. The *poly*-films were deposited at 200 °C, whereas the *spc*-films were prepared by postannealing *a*-films at 250 °C in a vacuum, which were deposited without intentional substrate heating (less than 60 °C). The fabrication process strongly influenced both the thermal and DH stability characteristics. 1) *Poly*-In<sub>2</sub>O<sub>3</sub>:Me films: They exhibited improved electrical properties with increased  $\mu$  and constant  $N$  after postannealing at temperatures greater than the deposition temperature in vacuum or N<sub>2</sub> atmosphere. Analysis of the Hall and SE measurements revealed that the improvement in  $\mu$  originates from an increase in intragrain mobility with a decrease in the GB potential barrier height.

Postannealing increased the crystallite sizes without any significant change in the grain structure. Therefore, the postannealing reduced the lattice defects within the grains and at the GBs produced by the low-temperature deposition. Moreover, the *poly*-films exhibited no degradation in electrical properties after the DH test. In addition, no changes in the inter- and intragrain mobilities were observed. XRD measurements revealed that the *poly*-films possessed in-plane compressive strains and the crystalline grains were densely packed, as observed in the SEM and TEM images. Therefore, there were no spaces for the water molecules to ingress through the GBs to influence the potential barrier for electrons. 2) *SpC*-In<sub>2</sub>O<sub>3</sub>:H and *spC*-In<sub>2</sub>O<sub>3</sub>:Me,H films: Postannealing at temperatures greater than 400 °C reduced both the *N* and  $\mu$  values with the effusion of H<sub>2</sub>O. The resulting *N* values were considerably less than those of the corresponding *poly*-films, wherein the Me impurities were considered to generate free carriers. Moreover, the GB potential barrier height increased as revealed by an analysis of the Hall and SE measurements. These results clearly demonstrate that diffusion of the H and OH to grain surfaces by high-temperature annealing produced the lattice defects inside the grains, leading to strong carrier compensation. In addition, the effusion of H<sub>2</sub>O from the films activated defects at the GBs, producing a large potential barrier for free electrons. On the other hand, the *spC*-films exhibit an increase in resistivity with DH time, due to a decrease in  $\mu$ . The deterioration increases with H content. An analysis of the Hall and SE measurements revealed that the reduction of  $\mu$  originates from an increase in the GB potential barrier height with negligible change in the intragrain properties. The difference in DH stability characteristics between the *spC*-films with low and high H can be explained by the different degrees of water-molecule ingress into the GBs caused by the spaces at the GBs. The *spC*-films with high H would possess thicker water-molecule layers at the GBs after the DH test than those with lower H due to the larger void spaces.

Based on these results, the *poly*- and *spC*-films should be used properly when applying high-mobility BB-TCOs to (opto)electronic devices, including thin-film transistors, photosensors, light-emitting devices, and photovoltaics. Certain devices must withstand metallization processes involving high temperatures up to 400–500 °C. In these devices, the *poly*-In<sub>2</sub>O<sub>3</sub>:Me layers are acceptable candidates. After the heat treatment, their optoelectrical properties improve further. Conversely, other devices require a low-temperature (less than 200 °C) process during and after TCO formation. The *spC*-In<sub>2</sub>O<sub>3</sub>:Me,H layers could be applied to such devices with encapsulation. Careful control of the H contents in as-deposited state is also required to mitigate the DH instability. Furthermore, films with mixed phases composed of a crystalline phase in an as-deposited state and crystallized phase after postannealing, fabricated by adjusting the growth temperature, can exhibit denser GB structures and superior stability characteristics when compared to the *spC*-films. Such films can also be used, based on the manufacturing process conditions of the applied devices.

## 4. Experimental Section

Approximately 60 and 220 nm thick In<sub>2</sub>O<sub>3</sub> films deposited on glass substrates and SiO<sub>2</sub>/Si substrates using an in-line RPD (Sumitomo Heavy Industries, URT-IP2) system were characterized.<sup>[58]</sup> The details of the film

fabrication were reported elsewhere.<sup>[16]</sup> Briefly, the films were deposited on the substrates moving in a transport direction. Ceramic tablets (Sumitomo Metal Mining) with different impurities were used, namely, pure In<sub>2</sub>O<sub>3</sub>, In<sub>2</sub>O<sub>3</sub> with a WO<sub>3</sub> content of 1 wt%, and In<sub>2</sub>O<sub>3</sub> with CeO<sub>2</sub> contents of 1, 2, and 3 wt%. The deposition gases were Ar, O<sub>2</sub>, and H<sub>2</sub>O at a total pressure of  $\approx 0.4$  Pa. The flow ratio of O<sub>2</sub> to Ar was fixed at 24%, whereas  $P_{\text{H}_2\text{O}}$  was varied from  $1 \times 10^{-5}$  to  $5 \times 10^{-4}$  Pa before deposition monitored by quadrupole mass spectrometry (Inficon, Transpector XPR3). The distance from the tablet surface to the substrate transfer line was  $\approx 60$  cm, and the distance to be deposited during transfer was  $\approx 30$  cm. For the fabrication of the *poly*-In<sub>2</sub>O<sub>3</sub>, In<sub>2</sub>O<sub>3</sub>:W, and In<sub>2</sub>O<sub>3</sub>:Ce films, the films were deposited at 200 °C. The heated substrate and growth surface suppressed the incorporation of a large amount of H into the film; however, they possessed H atoms in the order of 0.2–0.5 at%. *a*-In<sub>2</sub>O<sub>3</sub>:H, In<sub>2</sub>O<sub>3</sub>:W,H, and In<sub>2</sub>O<sub>3</sub>:Ce, H films were fabricated without intentional substrate heating. The maximum substrate temperatures were observed to be less than 60 °C during deposition using thermolabels attached to the glass and SiO<sub>2</sub>/Si substrates. *SpC*-In<sub>2</sub>O<sub>3</sub>:H, In<sub>2</sub>O<sub>3</sub>:W,H, and In<sub>2</sub>O<sub>3</sub>:Ce,H films were prepared by postannealing the corresponding *a*-films at 250 °C in a vacuum. The H contents were in the order of 1.5 and 4.0 at% in the initial *a*-films, and  $\approx 10\%$  of the H content was effused from the films during crystallization.<sup>[16]</sup>

The notation of *poly*-In<sub>2</sub>O<sub>3</sub>:Me was used here instead of *poly*-In<sub>2</sub>O<sub>3</sub>:Me, H because it was found that the influence of H in the Me-doped films on their electrical properties was minor when compared to the *spC*-films. However, the effect cannot be ignored, as clearly observed in the *poly*-In<sub>2</sub>O<sub>3</sub> films described in Section 2. The notations of In<sub>2</sub>O<sub>3</sub>:Me,H and In<sub>2</sub>O<sub>3</sub>:H were used for the amorphous and crystallized films because the H within the films largely influenced their structural and optoelectrical properties. The notation of *spC*- was used instead of *poly*- to stress the difference in polycrystalline films prepared by solid-phase crystallization and conventional vapor-phase crystal growth.

The thermal stabilities of the  $\approx 220$  nm thick and 60 nm thick films were tested through Hall-*T* measurements (Toyo, ResiTest8300) in a vacuum ( $10^{-3}$ – $10^{-2}$  Pa) and postannealing at temperatures of 300, 400, and 500 °C for 30 min in an N<sub>2</sub> atmosphere with a heating and cooling rate of 20 °C min<sup>-1</sup>, respectively. The Hall-*T* measurements in van der Pauw configurations<sup>[74]</sup> were performed every 20 °C during the heating and subsequent cooling processes (40–300–40, 40–400–40, and 40–500–40 °C). It required 16 h for a Hall-*T* measurement between 40 and 300 °C, and 30 h for a Hall-*T* measurement between 40 and 500 °C. The values of  $\rho$ , *N*, and  $\mu$  of the films after the Hall-*T* measurements or postannealing were measured at room temperature. A knowledge of the variations under different annealing conditions is useful to understand the degree of stability of the materials. The DH stability of the films was tested through DH treatment (Espec, LHL-113) at 85 °C and 85% relative humidity up to 1000 h. The surface morphology and crystallinity of the films were analyzed by SEM (Hitachi, S-4300) and XRD (Rigaku, SmartLab), respectively. Desorption gases from the films during heating in a vacuum were evaluated by TDS (Esco, EMD-1000S) using 220 nm thick films on SiO<sub>2</sub>/Si. H<sub>2</sub>O ( $m/z = 18$ , where  $m/z$  indicates the molecular mass to charge ratio), O<sub>2</sub> ( $m/z = 32$ ), and In ( $m/z = 115$ ) were monitored. *a*-films were characterized instead of *spC*-films, because the signals from the *a*-films included information of the desorption gasses during both solid-phase crystallization and annealing of the crystallized films at higher temperatures. The  $N_{\text{opt}}$  and  $\mu_{\text{opt}}$  of the films were evaluated by SE. SE spectra were measured from UV to IR wavelengths using two rotating-compensator ellipsometry systems, one operating at 200–1700 nm (J. A. Woolam, M-2000) and the other operating from 1.7 to 30  $\mu\text{m}$  (J. A. Woolam, IR-VASE). Here, the  $\approx 60$  nm thick films were characterized instead of the 220 nm thick films because thinner films are beneficial for SE fitting due to the minor effects of optical interference and thickness-dependent properties on the optical analysis. Details on the measurement and data analysis procedures can be found elsewhere.<sup>[25]</sup>

## Supporting Information

Supporting Information is available from the Wiley Online Library or from the author.

## Acknowledgements

T.K. thanks Junichi Nomoto for characterization of *poly*-films by XRD and Fumio Kawamura, Jiro Nishinaga, and Hitoshi Tampo for fruitful discussions. This work was supported partly by the National Institute of Advanced Industrial Science and Technology (AIST), the New Energy and Industrial Technology Development Organization (NEDO) under the Ministry of Economy, Trade and Industry (METI), Japan, and JSPS KAKENHI Grant Number JP20K05339.

## Conflict of Interest

The authors declare no conflict of interest.

## Keywords

60 years of *pss*, damp heat degradation, indium oxide, mobility, stability, transparent conductive oxides

Received: July 28, 2020

Revised: December 1, 2020

Published online: January 15, 2021

- [1] T. J. Coutts, D. L. Young, T. A. Gessert, in *Handbook of Transparent Conductors* (Eds: D. Ginley, H. Hosono, D. C. Paine), Springer, Boston **2011**.
- [2] A. E. Delahoy, S. Guo, in *Handbook of Photovoltaic Science and Engineering* (Eds: A. Luque, S. Hegedus), 2nd ed., Wiley, Chichester **2011**.
- [3] T. Koida, in *Spectroscopic Ellipsometry for Photovoltaics, Vol. 1, Fundamental Principles and Solar Cell Characterization* (Eds: H. Fujiwara, R. W. Collins), Springer, Berlin **2018**.
- [4] I. Hamberg, C. G. Granqvist, *J. Appl. Phys.* **1986**, *60*, R123.
- [5] C. H. Yi, Y. Shigesato, I. Yasui, S. Takaki, *Jpn. J. Appl. Phys., Part 2 Lett.* **1995**, *34*, L244.
- [6] R. Bel Hadj Tahar, T. Ban, Y. Ohya, Y. Takahashi, *J. Appl. Phys.* **1998**, *83*, 2631.
- [7] T. Minami, T. Kakumu, S. Takata, *J. Vac. Sci. Technol. A* **1996**, *14*, 1704.
- [8] A. Kaijo, K. Inoue, S. Matsuzaki, Y. Shigesato, in *PRICM 4 Fourth Pacific Rim Int. Conf. Adv. Mater. Process, Vol. I/II*, The Japan Institute of Metals and Materials, Sendai, Japan **2001**, pp. 1787–1790.
- [9] A. E. Delahoy, S. Y. Guo, *J. Vac. Sci. Technol. A* **2005**, *23*, 1215.
- [10] M. F. A. M. Van Hest, M. S. Dabney, J. D. Perkins, D. S. Ginley, M. P. Taylor, *Appl. Phys. Lett.* **2005**, *87*, 10.
- [11] T. Asikainen, M. Ritala, M. Leskela, *Thin Solid Films* **2003**, *440*, 152.
- [12] T. Koida, M. Kondo, *J. Appl. Phys.* **2007**, *101*, 063705.
- [13] G. H. Wang, C. Y. Shi, L. Zhao, H. W. Diao, W. J. Wang, *Appl. Surf. Sci.* **2017**, *399*, 716.
- [14] Y. Meng, X. L. Yang, H. X. Chen, J. Shen, Y. M. Jiang, Z. J. Zhang, Z. Y. Hua, *Thin Solid Films* **2001**, *394*, 218.
- [15] P. F. Newhouse, C. H. Park, D. A. Keszler, J. Tate, P. S. Nyholm, *Appl. Phys. Lett.* **2005**, *87*, 1121084.
- [16] T. Koida, Y. Ueno, H. Shibata, *Phys. Status Solidi* **2018**, *215*, 1700506.
- [17] E. Kobayashi, Y. Watabe, T. Yamamoto, *Appl. Phys. Express* **2015**, *8*, 015505.
- [18] T. Koida, H. Fujiwara, M. Kondo, *Jpn. J. Appl. Phys.* **2007**, *46*, L685.
- [19] C. Warmstrong, Y. Yoshida, D. W. Readey, C. W. Teplin, J. D. Perkins, P. A. Parilla, L. M. Gedvilas, B. M. Keyes, D. S. Ginley, *J. Appl. Phys.* **2004**, *95*, 3831.
- [20] T. Koida, H. Fujiwara, M. Kondo, *J. Non-Cryst. Solids* **2008**, *354*, 2805.
- [21] O. Bierwagen, *Semicond. Sci. Technol.* **2015**, *30*, 1.
- [22] N. Preissler, O. Bierwagen, A. T. Ramu, J. S. Speck, *Phys. Rev. B* **2013**, *88*, 085305.
- [23] T. Koida, M. Kondo, *J. Appl. Phys.* **2007**, *101*, 063713.
- [24] Y. Yoshida, D. M. Wood, T. A. Gessert, T. J. Coutts, *Appl. Phys. Lett.* **2004**, *84*, 2097.
- [25] T. Koida, M. Kondo, K. Tsutsumi, A. Sakaguchi, M. Suzuki, H. Fujiwara, *J. Appl. Phys.* **2010**, *107*, 033514.
- [26] S. Calnan, A. N. Tiwari, *Thin Solid Films* **2010**, *518*, 1839.
- [27] J. E. Medvedeva, *Phys. Rev. Lett.* **2006**, *97*, 086401.
- [28] D. S. Bhachu, D. O. Scanlon, G. Sankar, T. D. Veal, R. G. Egdel, G. Cibir, A. J. Dent, C. E. Knapp, C. J. Carmalt, I. P. Parkin, *Chem. Mater.* **2015**, *27*, 2788.
- [29] J. Xu, J. B. Liu, B. X. Liu, S. N. Li, S. H. Wei, B. Huang, *Adv. Electron. Mater.* **2018**, *4*, 1700553.
- [30] J. E. N. Swallow, B. A. D. Williamson, S. Sathasivam, M. Birkett, T. J. Featherstone, P. A. E. Murgatroyd, H. J. Edwards, Z. W. Lebens-Higgins, D. A. Duncan, M. Farnworth, P. Warren, N. Peng, T. L. Lee, L. F. J. Piper, A. Regoutz, C. J. Carmalt, I. P. Parkin, V. R. Dhanak, D. O. Scanlon, T. D. Veal, *Horizons* **2020**, *7*, 236.
- [31] X. Wu, *Sol. Energy* **2004**, *77*, 803.
- [32] J. A. Anna Selvan, A. E. Delahoy, S. Guo, Y. M. Li, *Sol. Energy Mater. Sol. Cells* **2006**, *90*, 3371.
- [33] A. E. Delahoy, L. Chen, M. Akhtar, B. Sang, S. Guo, *Sol. Energy* **2004**, *77*, 785.
- [34] B. Macco, Y. Wu, D. Vanhemel, W. M. M. Kessels, *Phys. Status Solidi RRL* **2014**, *8*, 987.
- [35] A. Nakane, S. Fujimoto, M. Tamakoshi, T. Koida, J. N. Hilfiker, G. E. Jellison Jr, T. N. Murakami, T. Miyadera, H. Fujiwara, in *Spectroscopic Ellipsometry for Photovoltaics Volume 2: Application and Optical Data of Solar Cell Materials* (Eds: H. Fujiwara, R. W. Collins), Springer, Berlin **2018**.
- [36] T. Koida, H. Fujiwara, M. Kondo, *Appl. Phys. Express* **2008**, *1*, 041501.
- [37] L. Barraud, Z. C. Holman, N. Badel, P. Reiss, A. Descoeudres, C. Battaglia, S. De Wolf, C. Ballif, *Sol. Energy Mater. Sol. Cells* **2013**, *115*, 151.
- [38] M. Taguchi, A. Yano, S. Tohoda, K. Matsuyama, Y. Nakamura, T. Nishiwaki, K. Fujita, E. Maruyama, *IEEE J. Photovoltaics* **2014**, *4*, 96.
- [39] E. Kobayashi, Y. Watabe, T. Yamamoto, Y. Yamada, *Sol. Energy Mater. Sol. Cells* **2016**, *149*, 75.
- [40] F. Meng, J. Shi, Z. Liu, Y. Cui, Z. Lu, Z. Feng, *Sol. Energy Mater. Sol. Cells* **2014**, *122*, 70.
- [41] J. Keller, A. Aijaz, F. Gustavsson, T. Kubart, L. Stolt, M. Edoff, T. Törndahl, *Sol. Energy Mater. Sol. Cells* **2016**, *157*, 757.
- [42] T. Koida, J. Nishinaga, Y. Ueno, H. Higuchi, H. Takahashi, M. Iioka, Y. Kamikawa, H. Shibata, S. Niki, *Prog. Photovoltaics Res. Appl.* **2019**, *27*, 491.
- [43] H. Sai, T. Matsui, K. Matsubara, *Appl. Phys. Lett.* **2016**, *109*, 183506.
- [44] E. Aydin, M. De Bastiani, X. Yang, M. Sajjad, F. Aljamaan, Y. Smirnov, M. N. Hedhili, W. Liu, T. G. Allen, L. Xu, E. Van Kerschaver, M. Morales-Masis, U. Schwingenschlögl, S. De Wolf, *Adv. Funct. Mater.* **2019**, *29*, 1901741.
- [45] Y. Jiang, T. Feurer, R. Carron, G. T. Sevilla, T. Moser, S. Pisoni, R. Erni, M. D. Rossell, M. Ochoa, R. Hertwig, A. N. Tiwari, F. Fu, *ACS Nano* **2020**, *14*, 7502.
- [46] D. Erfurt, T. Koida, M. D. Heinemann, C. Li, T. Bertram, J. Nishinaga, B. Szyszka, H. Shibata, R. Klenk, R. Schlattmann, *Sol. Energy Mater. Sol. Cells* **2020**, *206*, 110300.
- [47] S. Li, Z. Shi, Z. Tang, X. Li, *J. Alloys Compd.* **2017**, *705*, 198.
- [48] E. Kobayash, N. Nakamura, Y. Watabe, in *Proc 27th European Photovoltaic Solar Energy Conference* (Eds: S. Nowak, A. Jager-Waldau, P. Helm), WIP, Frankfurt, Germany **2012**, pp. 1619–1623.
- [49] Y. Shimura, K. Nomura, H. Yanagi, T. Kamiya, M. Hirano, H. Hosono, *Thin Solid Films* **2008**, *516*, 5899.



- [50] R. H. Horng, D. S. Wu, Y. C. Lien, W. H. Lan, *Appl. Phys. Lett.* **2001**, 79, 2925.
- [51] A. Ingenito, G. Nogay, Q. Jeangros, E. Rucavado, C. Allebé, S. Eswara, N. Valle, T. Wirtz, J. Horzel, T. Koida, M. Morales-Masis, M. Despeisse, F. J. Haug, P. Löper, C. Ballif, *Nat. Energy* **2018**, 3, 800.
- [52] L. Tutsch, F. Feldmann, J. Polzin, C. Luderer, M. Bivour, A. Moldovan, J. Rentsch, M. Hermle, *Sol. Energy Mater. Sol. Cells* **2019**, 200, 109960.
- [53] T. Koida, H. Sai, H. Shibata, M. Kondo, in *19th Int. Work. Act. Flatpanel Displays Devices*, IEEE, Piscataway, NJ **2012**, pp. 44–48.
- [54] T. Tohsophon, A. Dabirian, S. De Wolf, M. Morales-Masis, C. Ballif, *APL Mater.* **2015**, 3, 116105.
- [55] G. C. E. Jost, A. N. Hamri, F. Köhler, J. Hüpkes, *Mater. Sci.* **2016**, 213, 1751.
- [56] T. Koida, *Phys. Status Solidi A* **2017**, 214, 1600464.
- [57] J. Nomoto, K. Inaba, S. Kobayashi, T. Watanabe, H. Makino, T. Yamamoto, *Materials* **2017**, 10, 916.
- [58] K. Iwata, T. Sakemi, A. Yamada, P. Fons, K. Awai, T. Yamamoto, S. Shirakata, K. Matsubara, H. Tampo, K. Sakurai, S. Ishizuka, S. Niki, *Thin Solid Films* **2005**, 480–481, 199.
- [59] R. Muydinov, A. Steigert, M. Wollgarten, P. P. Michałowski, U. Bloeck, A. Pflug, D. Erfurt, R. Klenk, S. Körner, I. Lauermann, B. Szyzka, *Materials* **2019**, 12, 266.
- [60] Y. Wu, B. Macco, D. Vanhemel, S. Ko, M. A. Verheijen, P. M. Koenraad, W. M. M. Kessels, F. Roozeboom, *ACS Appl. Mater. Interfaces* **2017**, 9, 592.
- [61] S. Limpijumnong, P. Reunchan, A. Janotti, C. G. Van De Walle, *Phys. Rev. B* **2009**, 80, 193202.
- [62] A. Samanta, J. B. Varley, V. Lordi, *Appl. Phys. Lett.* **2020**, 117, 062103.
- [63] P. Agoston, K. Albe, *Phys. Rev. B* **2011**, 84, 045311.
- [64] M. Wagner, P. Lackner, S. Seiler, A. Brunsch, R. Bliem, S. Gerhold, Z. Wang, J. Osiecki, K. Schulte, L. A. Boatner, M. Schmid, B. Meyer, U. Diebold, *ACS Nano* **2017**, 11, 11531.
- [65] T. Koida, H. Shibata, M. Kondo, K. Tsutsumi, A. Sakaguchi, M. Suzuki, H. Fujiwara, *J. Appl. Phys.* **2012**, 111, 063721.
- [66] J. B. Varley, H. Peelaers, A. Janotti, C. G. Van De Walle, *J. Phys. Condens. Matter* **2011**, 23, 334212.
- [67] B. Macco, H. C. M. Knoop, W. M. M. Kessels, *ACS Appl. Mater. Interfaces* **2015**, 7, 16723.
- [68] H. F. Wardenga, M. V. Frischbier, *Materials* **2015**, 8, 561.
- [69] T. Koida, M. Kondo, *J. Appl. Phys.* **2006**, 99, 123703.
- [70] M. V. Frischbier, H. F. Wardenga, M. Weidner, O. Bierwagen, J. Jia, Y. Shigesato, A. Klein, *Thin Solid Films* **2016**, 614, 62.
- [71] R. L. Petritz, *Phys. Rev.* **1956**, 104, 1508.
- [72] L. L. Kazmerski, W. B. Berry, C. W. Allen, *J. Appl. Phys.* **1972**, 43, 3515.
- [73] J. Hüpkes, J. I. Owen, M. Wimmer, F. Ruske, D. Greiner, R. Klenk, U. Zastrow, J. Hotovy, *Thin Solid Films* **2014**, 555, 48.
- [74] T. Koida, T. Kaneko, H. Shibata, *Materials* **2017**, 10, 141.